THE SOLAR CORONA AS PROBED BY COMET LOVEJOY (C/2011 W3)

J. C. Raymond[1], P. I. McCauley[1], S. R. Cranmer[1], and C. Downs[2]
[1] Harvard-Smithsonian Center for Astrophysics, 60 Garden St, Cambridge, MA 02138, USA
[2] Predictive Sciences, Inc., 990 Mesa Rim Rd., Suite 170, San Diego, CA, 92121, USA

ABSTRACT

Extreme-ultraviolet images of Comet Lovejoy (C/2011 W3) from the Atmospheric Imaging Assembly show striations related to the magnetic field structure in both open and closed magnetic regions. The brightness contrast implies coronal density contrasts of at least a factor of six between neighboring flux tubes over scales of a few thousand kilometers. These density structures imply variations in the Alfvén speed on a similar scale. They will drastically affect the propagation and dissipation of Alfvén waves, and that should be taken into account in models of coronal heating and solar wind acceleration. In each striation, the cometary emission moves along the magnetic field and broadens with time. The speed and the rate of broadening are related to the parallel and perpendicular components of the velocities of the cometary neutrals when they become ionized. We use a magnetohydrodynamic model of the coronal magnetic field and the theory of pickup ions to compare the measurements with theoretical predictions, in particular with the energy lost to Alfvén waves as the cometary ions isotropize.

1. INTRODUCTION

Extreme Ultraviolet (EUV) images of Comet Lovejoy (C/2011 W3) obtained with the Atmospheric Imaging Assembly (AIA) instrument on the *Solar Dynamics Observatory* (*SDO*) show a tail that consists of a remarkable series of striations a few arcseconds across at an angle to the comet's path. Those striations change direction abruptly along the trajectory, and Downs et al. (2013) showed that they align with the magnetic field based on magnetohydrodynamic (MHD) simulations with the thermodynamic version of the Magnetohydrodynamic Algorithm on a Sphere (MAS) code. McCauley et al. (2013) showed that the positions, lengths, and relative intensities of the tail as seen in the various AIA filters agree with the theory that the emission arises from cometary gas as it is ionized through successive ionization states (Bryans & Pesnell 2012), with most of the wavelength bands dominated by emission from oxygen. McCauley et al. (2013) were able to determine the outgassing rate of the comet and the relative abundances of carbon, oxygen, and iron.

In this paper we investigate the striations further. We use them to probe the structure of the corona at a single position along the comet's trajectory, rather than relying on a line-of-sight average as is typical of most remote sensing observations (Raymond et al. 1998; Uzzo et al. 2001; Ciaravella et al. 2010). In particular, we interpret the striations as magnetic flux tubes containing relatively high densities such that neutral H and O atoms from the comet travel with the comet through the low-density plasma between the dense tubes. When they reach a denser region, they become ionized and confined to the flux tube, traveling along it but unable to cross field lines. The lack of emission between the striations requires that few of the neutrals released from the comet in those regions become ionized in the time it takes the comet to cross, while most of the neutrals released within a striation become ionized. That implies ionization times, and hence densities, for the high- and low-density flux tubes.

Fine structure in the corona has been seen earlier in processed eclipse images as filaments 1000–5000 km across (November & Koutchmy 1996; Woo 2007). While the observed contrast

level is small, the corona is optically thin and the path length is large, so that November & Koutchmy estimated a local density contrast of $\Delta n/n = 100\%$. We show that the density contrast we derive is compatible with the eclipse observations. On larger scales, polar plumes stand out above the background (Tian et al. 2011), and they have similar density contrasts (Young et al. 1999).

The small-scale density structure has important implications for the propagation and dissipation of Alfvén waves. Sharp gradients in Alfvén speed cause rapid dispersion and phase mixing, converting the waves to shorter wavelength modes that can damp rapidly (Lee & Roberts 1986; Evans et al. 2012). Density gradients can also give rise to entirely different modes such as drift waves, especially if velocity shear is present, and they might play a role in coronal heating (Saleem et al. 2012). If the solar wind mass flux remains roughly constant across the striations, then regions of high (low) density will be correlated with regions of low (high) radial velocity. In such highly sheared regions, it has been shown that some fraction of an incoming Alfvén wave train can be transformed into a compressive, longitudinal form similar to a fast-mode MHD wave (e.g., Nakariakov et al. 1998; Gogoberidze et al. 2007; Hollweg et al. 2013)

We compare the observed scale of the striations with predictions for the energy-containing scales (the scales of the waves that contain most of the power and cascade to smaller scales to deposit their energy), which are central to models of coronal heating (Abramenko et al. 2013; Cranmer & van Ballegooijen 2005; Hollweg et al. 2010). While we concentrate on an open field region of slow solar wind, we also consider a closed field region.

An important aspect of the interaction of the oxygen ions with the magnetic field is that they behave as pickup ions (Moebius et al. 1985). We use the velocity of the comet and the direction of the magnetic field from the MHD model of Downs et al. (2013) to calculate the velocity components parallel and perpendicular to the magnetic field. To compute the speed of the cometary plasma along the field direction and its rate of spreading, we assume that the particles relax to a bispherical
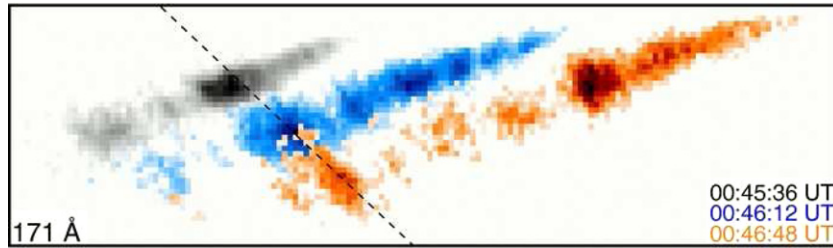
Figure 1. Three co-aligned AIA images in the 171 Å band taken 36 s apart. They show the centroid motion and the spreading of the emitting plasma along the magnetic field. The background coronal emission has been removed based on pre- and post-comet images. (Adapted from McCauley et al. 2013.)

(A color version of this figure is available in the online journal.)

distribution according to the theory of Williams & Zank (1994). We then compare those predictions with the observations.

In the following sections, we briefly summarize the properties of Comet Lovejoy, discuss the AIA observations and analyze their implications for the coronal density structure, calculate the predicted velocity and velocity spread along the magnetic field, discuss the implications for MHD wave propagation, and summarize our findings.

2. COMET LOVEJOY

Comet Lovejoy is the largest member of the Kreutz family of sungrazing comets (Marsden 2005) seen in several decades. It reached perihelion at about 1.2 $R_\odot$ on 2011 December 16 and survived for 1.6 days afterward before the nucleus disintegrated. The disruption was probably due to thermal stresses in the comet interior (Sekanina & Chodas 2012). The diameter of the nucleus was estimated to be around 600 m before it approached the Sun (McCauley et al. 2013).

At heliocentric distances above about 3 $R_\odot$, Comet Lovejoy displayed a bright dust tail, but at smaller distances the dust grains sublimate quite rapidly and the dust tail disappeared (Sekanina & Chodas 2012), as is generally seen in sungrazing comets (Biesecker et al. 2002; Knight et al. 2010). However, a different tail visible in the ultraviolet (UV) and EUV channels of the AIA instrument was seen close to the Sun. As described by Bryans & Pesnell (2012), most of the AIA wavelength bands contain some lines of ionized oxygen along with the lines of highly ionized iron they were designed to capture. As the oxygen produced by photodissociation of water from the comet proceeds through the successive ionization stages, it emits photons in those bands. McCauley et al. (2013) showed that at coronal temperatures, each oxygen ion emits a fixed number of photons in each AIA band before it is ionized, so that it is simple to compute the number of O atoms released per second from the brightness in the AIA images. The AIA 1600 Å band is dominated by C IV rather than any O ion, and some emission from Fe in the AIA 171 Å band was indicated by comparison with the 131 Å and 193 Å bands, which are dominated by emission from the same O ions present in the 171 Å band (O V and O VI). It was possible to match the relative count rates in the different bands to within about a factor of two, derive the relative abundances of C, O, and Fe, and determine the outgassing rate. At the time of peak brightness, at about 00:46 UT, McCauley et al. (2013) derived an outgassing rate of about 3×10^{32} oxygen atoms per second, for a mass loss rate of about 9×10^6 g s^{-1}.

3. OBSERVATIONS

The AIA observations are presented in McCauley et al. (2013) and Downs et al. (2013). A set of images was obtained every
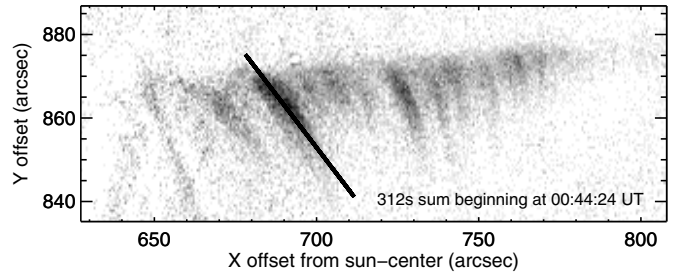

Figure 2. Sum of 26 2 s AIA 171 Å images taken over 312 s. The black line indicates the direction adopted for the striation in the subsequent figures. Intensities are extracted parallel and perpendicular to this direction. Note that the direction changes with position along the X-axis and that some of the striations curve, so that the contrast between on- and off-striation regions is washed out at X offsets above about 730″.

12 s with 0″.6 pixels for a spatial resolution of 1″.5 (Lemen et al. 2012). For the analysis here, we confine ourselves to the 171 Å band. The striations can be seen most clearly in that band because of its large effective area and the strong O V, O VI, and Fe IX lines in the bandpass. In addition, the ionization times of those ions are longer than the ionization times of the lower ions that dominate the other wavelength bands, so the striations are longer in the 171 Å band. We analyze images obtained near 00:46 UT, when the comet was about 1.3 $R_\odot$ from Sun center.

Figure 1, which reproduces part of Figure 3 of McCauley et al. (2013), is a superposition of three images in the AIA 171 Å band at intervals of 36 s. It clearly shows how the emission in each individual striation moves along the magnetic field and spreads along the field with time. In order to estimate the densities inside and outside of the striations, we will use the intensity contrast. In order to study the pickup ion behavior of the oxygen ions, we will use the speed along the magnetic field and the rate of spreading.

Figure 2 shows the sum of 26 2 s exposures obtained over 312 s, beginning at 00:44:24 UT during comet egress. Since the ionized plasma from the comet moves along magnetic field lines, the striations show the field line structure. The curvature seen in some of the striations could be partly due to intrinsic curvature of the field lines, but it may be largely due to relaxation of the field lines after they are perturbed by the ram pressure of the cometary gas.

Figure 3 shows images of the comet in the right panels and corresponding plots of the intensities along the lines cutting across the striations in the left panels. The top row shows the intensities for an image during ingress while the lower two rows show the intensities for two times during egress. The intensity contrast is a factor of two to three and the separation between striations is about 5″, or 4000 km, in the egress images. That contrast may be something of an underestimate due to the
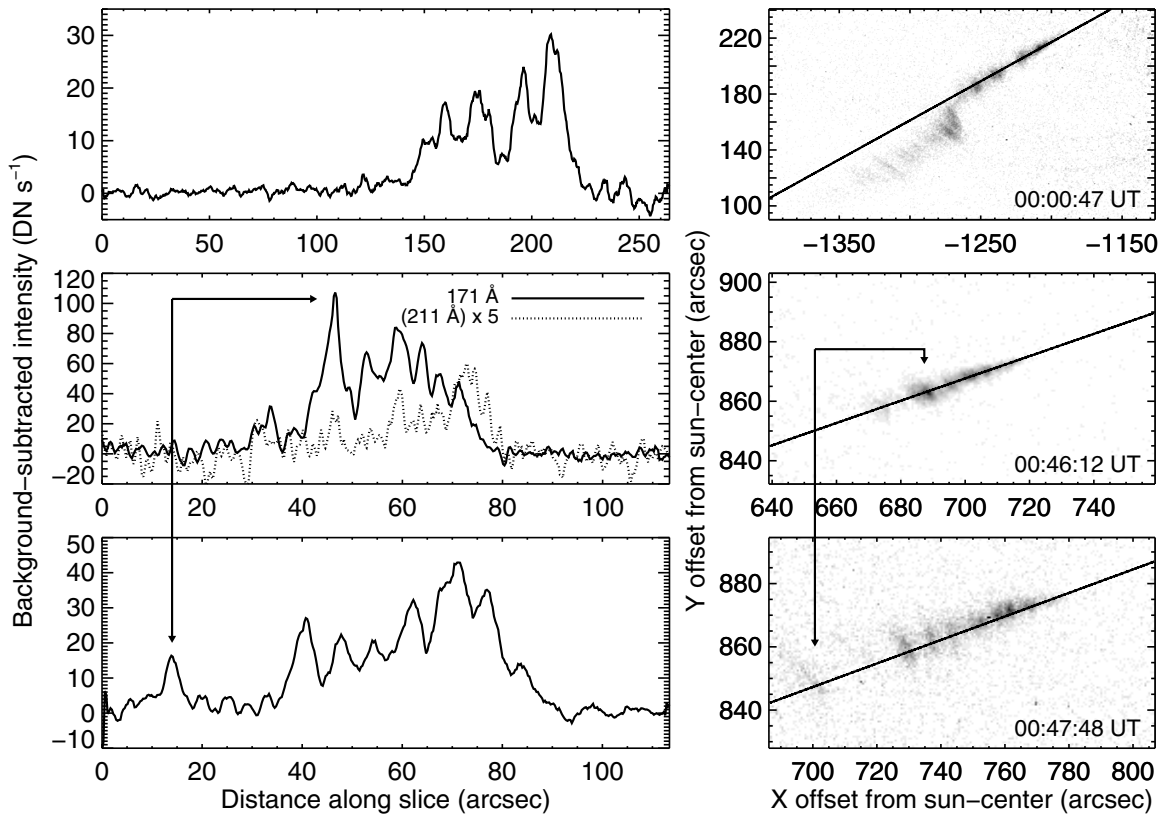
Figure 3. Intensity cuts perpendicular to the striations during ingress (top row) and at two times during egress (bottom two rows). The arrows in the bottom panels indicate the bright blob chosen for the striation direction in Figure 2 and the profiles shown in Figures 4 and 5.

instrumental resolution of $1''.5$, so the factor of two to three is a lower limit. The filling factor of the striations is about $1/2$, but that may also be influenced by the instrumental resolution. The amplitude of the brightness fluctuations in the ingress image is similar, but the separations are larger and less regular. The analysis in the following sections will concentrate on the egress observations, but we will return briefly to the ingress observation below.

The top panel in Figure 4 shows the extent of the brightest striation (indicated by the arrows in Figure 3) along its axis at each time. The values shown are FWHM widths of the brightness distribution along the filament. The width grows with time due to the spread of the ion velocities along the magnetic field. At later times the width saturates as the emission becomes very faint. The slope of the width versus time plot is $0''.224 \text{ s}^{-1}$, or 159 km s^{-1} in the plane of the sky. The lower panel shows the centroid position of the emission. The slope gives the plane-of-sky projection of the velocity along the magnetic field. The value of $0''.216 \text{ s}^{-1}$ corresponds to 154 km s^{-1}. From the magnetic field vector and the line-of-sight direction (Downs et al. 2013), we find that the measured (projected) values are 0.82 times the actual deprojected values. Therefore, $V_{\parallel} = 183 \text{ km s}^{-1}$ and the emitting region spreads at 200 km s^{-1}. Figure 5 shows the intensity profiles along the striation at several times as the emission spreads along the magnetic field.

4. ANALYSIS

We have chosen the observations during egress at about 00:44.5 UT for detailed analysis. According to the MAS models, this is an open field region where the coronal plasma flows at
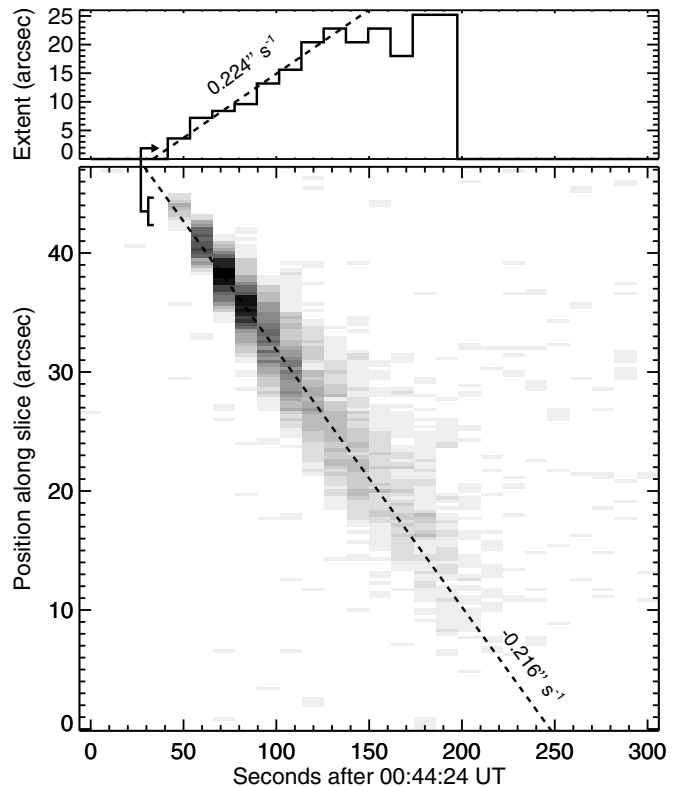
Figure 4. FWHM extent (top panel) and centroid (lower panel) of the emission in the AIA 171 Å band as a function of time, measured along the striation as shown in Figure 2. These characterize the rate at which the emission region spreads (top) and the speed at which the plasma travels along the magnetic field (bottom).
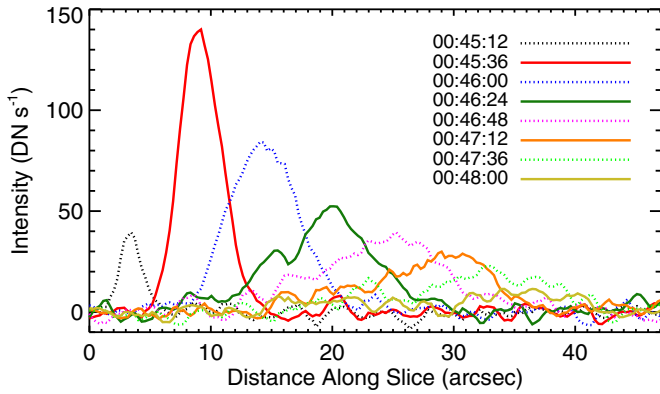
Figure 5. Profiles of the AIA intensity along the striation indicated in Figure 2. The motion along the striation and its increasing extent are apparent. The profile at 00:45:36 is close to Gaussian, while subsequent profiles are more skewed.

(A color version of this figure is available in the online journal.)

43 km s^{-1}. That speed indicates that this is a slow solar wind region.

4.1. Density Contrast

The striations are clearly aligned with the local magnetic field (McCauley et al. 2013; Downs et al. 2013). They are quasi-periodic, which might suggest a periodic source from the comet, and Figure 7 of McCauley et al. (2013) shows that the outgassing rate varies with time. However, the comet travels from one striation to the next in about 9 s, and it is not plausible that the comet rotates that rapidly. Nine seconds is much less than the critical rotation period for disruption of around half an hour (Jewitt 1997) and much less than observed comet rotation periods of hours to days. Instead, the striations arise because neutrals are not tied to the magnetic field, while ions are. The comet produces water at a rate of 3×10^{32} molecules per second near the brightness peak at 00:49 UT (McCauley et al. 2013). Photodissociation quickly splits the molecules into H and O atoms which share the comet's motion and form a cloud that expands at a few km s^{-1} (Combi 1996) as it travels at 530 km s^{-1} through the corona. The atoms travel freely until they become ionized and trapped on a field line.

We can obtain an upper limit to the density between striations from the intensity contrast and the condition that few of the cometary atoms are ionized in the inter-striation plasma. The comet crosses one of these 4$''$ regions in about 5 s. The ionization rate coefficients of H and O atoms are 2.9×10^{-8} and 8.7×10^{-8} n_e cm^3 s^{-1}, respectively, at temperatures of 1.5–2 MK according to the rates of Dere (2007) as given by version 7.1 of CHIANTI (Dere et al. 1997; Landi et al. 2013). Ionization can also occur by way of charge transfer with protons in the corona. For H and O atoms the rate coefficients $n_p V_{\rm comet} \sigma$ are 8.5×10^{-8} and 3.5×10^{-8} n_p cm^3 s^{-1} for a speed of 530 km s^{-1} based on cross sections of Schultz et al. (2008) and Phaneuf et al. (1987). Thus the total ionization rate coefficients for both H and O are about 1.2×10^{-7} cm^3 s^{-1}. The condition that fewer than 30% of the atoms are ionized between striations ($t_{\rm cross} < 0.3 t_{\rm ion}$) translates into an upper limit of 2.7×10^6 cm^{-3} on the coronal density between the striations.

On the other hand, most of the atoms are ionized in the striations. In order for 90% of the atoms from the comet to become ionized within a striation, the crossing time has to be at least twice the ionization time, $t_{\rm cross} > 2 t_{\rm ion}$. That implies a density of at least 1.7×10^7 cm^{-3} within the striations. Thus

the density contrast must be at least a factor of six. We note that if the striations occupy about half the space surrounding the comet and have densities near this limit, the average density is around 8×10^6 cm^{-3}. The MAS model predicts a density of 2.6×10^6 cm^{-3} at the point along the comet's path corresponding to the AIA image at 00:45:36 UT, but we will argue below that the magnetic field direction in is better agreement with the position which the comet reached 2–3 minutes earlier, and the predicted density there is 6.7×10^6 cm^{-3}, in reasonable agreement with our estimated average density. This shift of two or three minutes corresponds to an offset of about 4° in solar longitude, which is quite reasonable given the uncertainty in the magnetic field at the solar surface used by the MAS model.

Another estimate of the density in the striations can be obtained from the emission measure (EM), the filling factor (f), and an estimate of the length scale through the corona (L), $n_e = ({\rm EM}/(Lf))^{1/2}$. McCauley et al. (2013) obtained an EM from the AIA images just outside the comet's tail of 1.9×10^{26} cm^{-5}. The filling factor appears to be about 0.5 based on the fraction of the tail included in the striations, and the length scale is roughly 0.6 $R_\odot$. Thus we estimate $n_e = 1.3 \times 10^8$ cm^{-3}. This is clearly an average for the high-density regions along the line of sight. Since the comet was not too far from the plane of the sky at that time, it may be a reasonable estimate, but the observations pertain to an open field region, and closed field loops along the line of sight could easily dominate the EM. Therefore, we take this to be an upper limit. This limit agrees well with the estimate of 1.4×10^8 cm^{-3} derived from the ionization time from O III to O VI by McCauley et al. (2013). The density derived from the ionization time includes the electrons liberated by ionizing hydrogen and oxygen from the comet, so we conclude that 1.4×10^8 cm^{-3} is a solid upper limit to the density in the striations before the comet's arrival, while a density of 1.7×10^7 cm^{-3} from the density contrast is a lower limit.

The real situation is complex, of course. The density of cometary atoms is large enough that, once they begin to ionize, they significantly increase the total density. However, the ions and electrons move away from the cloud of neutrals at over 150 km s^{-1}. Another complication is the uncertainty in the electron temperature. Ionization by electrons continues as long as the electrons remain hot. Each ionization requires the ionization potential of 13.6 eV, and roughly 16 eV is lost in photons produced by collisional excitation. Moreover, the total thermal energy is shared among an increased number of electrons, rapidly reducing the temperature, so that each coronal electron can ionize only three or four cometary atoms unless additional heat is supplied. There is plenty of energy available in the cometary ions, so it is likely that the electron temperature is maintained by Coulomb collisions with ions. A detailed calculation is beyond the scope of this paper, but an electron temperature of 1–2 MK is consistent with the ionization times inferred from the relative intensities in the different AIA bands and with the X-rays detected with the X-Ray Telescope instrument on *Hinode* (McCauley et al. 2013).

4.2. Nature of the Density Structure

The cause of the inhomogeneous coronal density structure is not yet clear. One possibility is that the variations in density originate at the footpoints of magnetic flux tubes and propagate upward. Intensity oscillations measured with off-limb EUV imaging and spectroscopy imply the presence of compressible MHD waves that appear channeled along polar

plumes (e.g., DeForest & Gurman 1988; Ofman et al. 1999; Krishna Prasad et al. 2012). These fluctuations have periods of order 10–20 minutes, and if they were slow-mode MHD waves ($V_{ph} \approx v_{wind} + c_s \approx 200$ km s^{-1}), they could have wavelengths of order 0.2–0.4 $R_\odot$. These temporal and spatial scales are larger than the resolved passage through the striations, so the comet would be expected to "sample" such oscillations as quasi-static structures. The measured off-limb density fluctuation ratio $\delta\rho/\rho_0$ is only of order 0.03–0.1, but line-of-sight integration effects are likely to wash out the true local fluctuation amplitude.

Another type of proposed upflowing density variation is the jet- or piston-like motion associated with Type II spicules. These features have been suggested as a major source of mass for the corona and solar wind (De Pontieu et al. 2011; Pereira et al. 2012), though Klimchuk (2012) argues that these upflows are probably a minor contributor. A related possibility is that mass is injected into specific flux tubes in the slow solar wind by reconnection of open and closed magnetic fields in the low corona (Schwadron et al. 1999; Antiochos et al. 2011). That model was advanced specifically for the slow solar wind, but we see similar striations in fast wind regions, such as just before the kink in the upper panel of Figure 3. Reconnection between open and closed magnetic flux also occurs in coronal holes, but one might expect different scale lengths and filling factors. Neither of the above impulsive-driving scenarios makes a clear prediction as to the size or filling factor of the high- and low-density regions.

Still another picture is that variations in the expansion factor of different flux tubes give rise to different rates of Alfvén wave reflection, turbulent cascade, and coronal heating. This in turn causes differences in the flow speeds and densities in neighboring flux tubes. Cranmer et al. (2013) found significant inter-tube variations in a model containing a dense grid of flux tubes that connected a high-resolution quiet-Sun magnetogram with the ecliptic plane. The model solved time-steady equations of mass, momentum, and energy conservation along each flux tube using a self-consistent description of non-WKB Alfvén wave reflection and turbulent heating. Each of the individual flux tube models was given identical lower boundary conditions at the photosphere, and they differed only in the radial dependence of magnetic field strength. Figure 6 shows a cut through the modeled set of flux tubes at a constant radius of $r = 1.3\ R_\odot$. At that height, the mean separation between neighboring flux tubes was 5100 km, and roughly 45% of the flux tubes exhibited nearest-neighbor separations less than the observed striation size of 4000 km. The minimum, mean, and maximum electron densities in this set of models were 1.1×10^6, 4.2×10^6, and 7.9×10^6 cm^{-3}. The ratio of the standard deviation to the mean density was 0.32, which implies a representative contrast factor of order three. The distribution of transverse scale sizes is roughly a power law, with no dominant scale that separates the densest flux tubes from their more rarefied surroundings.

It is also within the realm of possibility that a sort of filamentation instability operates, based perhaps on the focusing of Alfvén waves into the lower Alfvén speed regions corresponding to higher density flux tubes. In quasi-steady flow models such as those of Champeaux et al. (1997), enhanced heating below the critical point in those flux tubes would further increase the density in those flux tubes. Nevertheless, it does appear to be possible that the observed striations could be the result (at least in part) of natural variations in the time-steady coronal heating
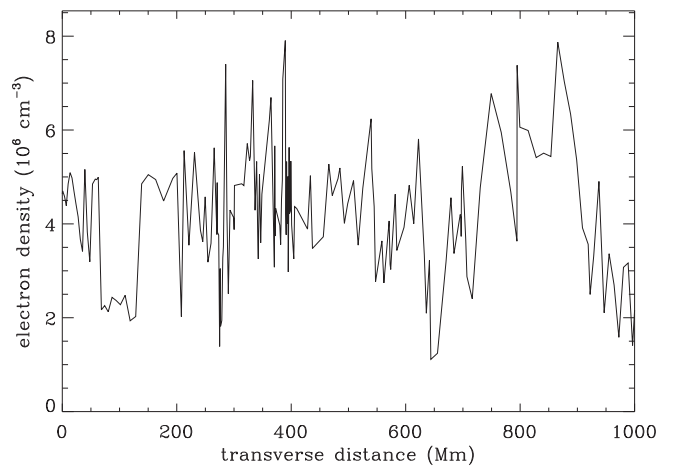
Figure 6. Modeled electron density plotted as a function of transverse distance along a set of magnetic flux tubes rooted in a low-latitude quiet Sun region observed in 2003 September by SOLIS. The densities were sampled at a constant radius of $r = 1.3\ R_\odot$ (see Cranmer et al. 2013).

and wind acceleration. In other words, it is not surprising that a highly structured magnetic field gives rise to a highly structured coronal plasma.

4.3. Pickup Ion Behavior

The cloud of neutral hydrogen and oxygen atoms produced by photodissociation of water moves with the comet and expands at a few km s^{-1}. When the atoms become ionized as they travel through the coronal magnetic field they behave as pickup ions (Williams & Zank 1994; Isenberg & Lee 1996). Initially they have velocity components $V_\parallel = V_{comet} \cos\theta$ and $V_\perp = V_{comet} \sin\theta$, where θ is the angle between the comet's trajectory and the magnetic field.

Since $V_\perp$ is the same for all the newly formed ions, they form a ring distribution in velocity space. The ring distribution is unstable, and it evolves into a bispherical shell in velocity space by emitting and absorbing Alfvén waves on a time scale of a few gyroperiods (Williams & Zank 1994). The bispherical shell is described in detail by Williams & Zank, and in particular the energy of the bispherical distribution is given by their Equation (4) as

$$E_{BD\pm} = \frac{nm\pi v_\pm^2}{a_T}\left[\frac{V_\parallel}{v_\pm}\left(V_\parallel V_A \pm V_A^2 \mp v_\pm^2\right) + \left(v_\pm^2 - V_A\right)^2\right],$$
(1)

where $v_\pm^2 \equiv V_\perp^2 + (V_\parallel \pm V_A)^2$, the areas of the sections of the bispherical shell are $a_\pm \equiv 2\pi v_\pm(v_\pm \mp V_\parallel - V_A)$, $a_T \equiv a_+ + a_-$, and of course V_A is the Alfvén speed. Under the assumption that the ions uniformly cover the bispherical shell, Equation (3) of Williams & Zank (1994) gives the bulk speed along the magnetic field.

To compare the predicted pickup ion behavior with observations, we use the MAS model predictions for the magnetic field direction and the Alfvén speed. That provides the parameters for the bispherical distribution and for the projection of the velocities onto the plane of the sky. We consider the position corresponding to the observation at 00:44.5 UT shown in Figures 1 through 5, where the comet was moving at 527 km s^{-1}, and where the high outgassing rate provided us with the best data.

The MAS model magnetic field at the 00:44.5 UT position lies only 3° from the direction perpendicular to the comet's motion, so that the predicted speed along the striation is only 24 km s^{-1}.

Table 1
Model and Observed Parameters

	Obs	Model 00:45.4 UT	Model 00:41.9 UT
$V_{com,x}$		392	385
$V_{com,y}$		347	362
$V_{com,z}$		31	45
B_x		0.29	0.34
B_y		−0.23	−0.11
B_z		−0.56	−0.50
n_e		2.6×10^6	6.7×10^6
V_A		878	480
$V_{s,POS}$	154	24	93
$V_{exp,POS}$	159	120	188
E_0		21880	22500
E_{BD}	8780	11840	13600

Note. Velocities in km s^{-1}, magnetic fields in G, density in cm^{-3}, and energies in eV per O atom.

However, the predicted direction of the field is changing rapidly in that region. In addition, the position of that rapid change is somewhat uncertain as a result of the uncertainty in the solar surface magnetic field that serves as a boundary condition, especially because the relevant region lies just behind the solar limb, and no magnetic field measurements exist for the back side of the Sun. Therefore, we also consider the coronal field predicted for a region that the comet passed 2.5 minutes earlier, at 00:41.9 UT. At that position the angle between the comet's orbit and the field was larger so that the predicted $V_\parallel$, while still lower than the observed value, is much more reasonable.

Table 1 lists the velocity components of the comet's motion and the components of the magnetic field in the Carrington coordinate system, along with the density and Alfvén speed, as predicted by the MAS model. It also compares the observed and predicted values of the bulk velocity and expansion velocity along the field in the plane of the sky ($V_{s,POS}$ and $V_{exp,POS}$, respectively) and the total kinetic energy (after deprojecting the plane-of-the-sky velocities) with the predicted energy of the bispherical distribution (E_0 and E_{BD}, respectively).

The predicted motion along the field for the comet position at 00:44.5 UT is far too small to match the observation, while that at 00:41.9 UT is closer to the observed value. This corresponds to a shift of about $4°$ in solar longitude. It still does not agree very well, and we consider that to be an indication that the angle between the comet trajectory and the field is larger than that given by the model. An increase of about $4°$ is required, depending on the projection onto the plane of the sky, and that is not unreasonable given the expected accuracy of the model.

The predicted expansion speed along the field line for the model parameters at 00:41.9 UT is somewhat larger than observed. We consider the comparison of the energy in the bispherical distribution to the initial kinetic energy to be the strongest test of the pickup ion theory. The observed value of E_{BD} depends on the deprojection of the centroid and expansion speeds, but those are not large corrections. The theory outlined above, taken with the Alfvén speed and angle between the comet motion and magnetic field direction, predicts $E_{BD}/E_0 = 0.60$, while the observed value is 0.39.

Coulomb collisions will transfer some energy from the oxygen ions to protons and electrons on a timescale comparable to the duration of our measurements. Table 2 lists the ionization times (t_{ion}), gyration periods (t_{Larmor}), and Coulomb collision times for transfer of energy among oxygen ions ($t_{O–O}$) and

Table 2
Collision and Gyration Timescales

	t_{ion}	t_{Larmor}	$t_{O–O}$	$t_{O–H}$
O$^+$	0.37	0.018	55600	1740
O^{2+}	0.89	0.009	3480	435
O^{3+}	2.6	0.006	686	193
O^{4+}	9.6	0.0045	217	109
O^{5+}	33.	0.0036	89	69

Note. Times in seconds.

between oxygen ions and protons ($t_{O–H}$) for the relevant O ions. Ionization times are from the work of Dere (2007), while Coulomb collision times are from Spitzer (1968). Coulomb collision times for O ions and electrons are comparable to those for O ions and protons, but we do not list them because we do not yet have firm predictions for the electron temperature. We assume a magnetic field of 0.6 G based on the MAS model and a density of 10^8 cm^{-3} based on the relative positions and lengths of the striations in the different AIA filters (McCauley et al. 2013). It is apparent that Coulomb losses might account for the difference between the observed and predicted values of E_{BD} and E_0, but a more detailed calculation of the evolution of the cloud of cometary ions is required.

5. DISCUSSION

We find that neighboring flux tubes show density variations of at least a factor of six on a scale of few thousand kilometers in an open field region at a height of about 1.3 $R_\odot$. While we have done a detailed analysis at only one position, similar striations are seen all along the comet's path. From Figure 1 of McCauley et al. (2013), there is an indication of wider separations at larger heliocentric heights. Earlier in the egress, when the comet was at a lower height, the tail was narrower and more continuous, presumably as a result of higher density in that region. The structure resembles that inferred from an edge-enhanced white light eclipse image by November & Koutchmy (1996), who also inferred a substantial density contrast.

It is unclear to what extent the small-scale striations elucidated in this paper relate to the larger-scale *polar plumes* that have been long known to exist in coronal holes. Plumes are bright ray-like features that trace out open magnetic field lines and exhibit a strong intensity contrast in off-limb images (e.g., Newkirk & Harvey 1968; Ahmad & Withbroe 1977; Suess 1982). Observational attempts to measure the density contrast between plumes and the more tenuous interplume corona have yielded different answers depending on the exact diagnostic techniques used. At heliocentric radii around 1.1–1.3 $R_\odot$, several analyses of the line-of-sight EUV and white-light emission have given density contrast ratios of order 3–6 (e.g., Saito 1965; Young et al. 1999). However, at similar heights, Orrall et al. (1990) combined the EUV and white-light data to estimate a statistical irregularity ratio $\langle n^2 \rangle / \langle n \rangle^2$. They inferred the presence of substantially higher contrast ratios of order 20–60. Orrall et al. concluded that there must be density fluctuations on spatial scales below their resolution of 5″–60″.

The inferred density contrast between flux tubes indicates variations in the Alfvén speed of at least factors of two to three. This points to the likelihood that large-scale MHD fluctuations will undergo rapid dispersion in the interface regions as they propagate along the field. When MHD waves pass through a strongly inhomogeneous background medium, their properties can be altered in a number of ways. Our understanding of these

transformations has been shaped by concepts from linear theory such as reflection (Heinemann & Olbert 1980; Chandran & Hollweg 2009), refraction (Stein 1971; Flå et al. 1984), and mode coupling (Valley 1974; Poedts et al. 1998; Mecheri & Marsch 2008). Further suggestions for the transformation and dissipation of wave energy—including phase mixing, shear-driven couplings, and various instabilities—were summarized in Section 1. It may also be the case that these kinds of mode conversions may be responsible for producing low-frequency compressive waves in coronal holes as observed recently by, e.g., Krishna Prasad et al. (2012) and Threlfall et al. (2013), since such waves are unlikely to travel far into the corona if they are produced only at the solar surface (Athay & White 1978).

The spatial scale of the cross-field striations revealed by Comet Lovejoy was roughly 4000 km at a heliocentric radius of ∼1.3 $R_\odot$. This demonstrates the presence of magnetic flux tubes with diameters at least an order of magnitude smaller than would exist if supergranular "funnels" were the smallest building blocks of coronal structure (see, e.g., Hackenberg et al. 2000). The observed spatial scale of 4000 km falls within the range of predictions of the perpendicular correlation length, or energy-containing length, in recent models of MHD turbulence. In these models, the turbulence is driven by the random-walk motions of kiloGauss-field intergranular bright points on the solar surface. Those bright points have horizontal scales of order 50–200 km in the photosphere (Berger & Title 2001; Abramenko et al. 2013). In the open flux tube models of Cranmer & van Ballegooijen (2005) and Cranmer et al. (2007), the correlation length $\lambda_\perp$ expands as the background field strength B decreases, with $\lambda_\perp \propto B^{-1/2}$. At heights of 1.2–1.4 $R_\odot$, the Cranmer & van Ballegooijen (2005) model gave $\lambda_\perp \approx$ 4900–6700 km, and the Cranmer et al. (2007) model gave $\lambda_\perp \approx$ 1250–1700 km. More recently, Cranmer & van Ballegooijen (2012) updated this model to include nonlinear effects that come to dominate in interplanetary space, and at 1.2–1.4 $R_\odot$, the revised values of $\lambda_\perp$ were found to be 2800–4300 km. Hollweg et al. (2010) showed that this range of correlation lengths is consistent with Faraday rotation fluctuations measured via radio sounding of spacecraft signals through the inner corona. The existence of density fluctuations on similar length scales is a predicted feature in both "passive scalar" extensions of MHD turbulence theory (e.g., Harmon & Coles 2005; Zank et al. 2012) and three-dimensional wave-driven models of the solar wind (Cranmer et al. 2013).

The images also allow us to test the theory of pickup ions. We measure a speed along the magnetic field of 154 km s^{-1} and a rate of spreading of 159 km s^{-1} in the plane of the sky. After correction for projection effects, the parallel speed is higher than expected from the comet velocity and the magnetic field direction. On the other hand, when those numbers and the Alfvén speed predicted by the MAS MHD model of Downs et al. (2013) are put into the Williams & Zank (1994) pickup ion model, the rate of spreading along the field line is below the predicted expansion rate. The total kinetic energy of the oxygen ions in the bispherical distribution is predicted to be about 60% of the initial oxygen atom kinetic energy, while 40% goes into waves. The observed kinetic energy is about two-thirds the expected value, quite likely because Coulomb equilibration with the protons from cometary H_2O has taken some energy from the oxygen. That will not affect V_{par}, but it will affect the rate of spreading along the magnetic field.

The MAS model predictions are in overall good agreement with the magnetic field directions and densities inferred from the comet images, as reported by Downs et al. (2013), provided that shifts along the comet's path corresponding to a few degrees in solar longitude are permitted. Considering that the models are based on a surface magnetic field that is measured over the course of a Carrington rotation and that the heating model currently used has substantial uncertainty, this is quite good agreement.

A detailed calculation of the electron temperature is beyond the scope of this paper. One complication is that the Alfvén speed changes as cometary gas is loaded onto the field lines, and another is that both cooling by excitation and ionization of the O ions and Coulomb heating are likely to be important. The Coulomb heating increases with charge state. When the oxygen is singly ionized, the collision time is 200 seconds, and Coulomb collisions could not maintain the electrons at 10^6 K against adiabatic expansion and radiative losses. However, the collision time drops as Z^2, so that Coulomb collisions could probably maintain that temperature in the region where the 171 Å emission arises. In addition, some of the wave energy produced during isotropization could heat the electrons (Cairns & Zank 2002).

REFERENCES

Abramenko, V. I., Zank, G. P., Dosch, A., et al. 2013, ApJ, 773, 167
Ahmad, I. A., & Withbroe, G. L. 1977, SoPh, 53, 397
Antiochos, S. K., Mikić, Z., Titov, V. S., Lionello, R., & Linker, J. A. 2011, ApJ, 731, 112
Athay, R. G., & White, O. R. 1978, ApJ, 226, 1135
Berger, T. E., & Title, A. M. 2001, ApJ, 553, 449
Biesecker, D. A., Lamy, P., St. Cyr, O. C., Llebaria, A., & Howard, R. A. 2002, Icar, 157, 323
Bryans, P., & Pesnell, W. D. 2012, ApJ, 760, 18
Cairns, I. H., & Zank, G. P. 2002, GeoRL, 29, 1143
Champeaux, S., Gazol, A., Passot, T., & Sulem, P.-L. 1997, ApJ, 486, 477
Chandran, B. D. G., & Hollweg, J. V. 2009, ApJ, 707, 1659
Ciaravella, A., Raymond, J. C., & Giordano, S. 2010, ApJL, 713, L69
Combi, M. R. 1996, Icar, 123, 207
Cranmer, S. R., & van Ballegooijen, A. A. 2005, ApJS, 156, 265
Cranmer, S. R., & van Ballegooijen, A. A. 2012, ApJ, 754, 92
Cranmer, S. R., van Ballegooijen, A. A., & Edgar, R. J. 2007, ApJS, 171, 520
Cranmer, S. R., van Ballegooijen, A. A., & Woolsey, L. N. 2013, ApJ, 767, 125
DeForest, C. E., & Gurman, J. B. 1998, ApJL, 501, L217
De Pontieu, B., McIntosh, S. W., Carlsson, M., et al. 2011, Sci, 331, 55
Dere, K. P. 2007, A&A, 466, 771
Dere, K. P., Landi, E., Mason, H. E., Monsignori-Fossi, B. C., & Young, P. R. 1997, A&AS, 125, 149
Downs, C., Linker, J. A., Mikić, Z., et al. 2013, Sci, 340, 1196
Evans, R. M., Opher, M., Oran, R., et al. 2012, ApJ, 756, 155
Flå, T., Habbal, S. R., Holzer, T. E., & Leer, E. 1984, ApJ, 280, 382
Gogoberidze, G., Rogava, A., & Poedts, S. 2007, ApJ, 664, 549
Hackenberg, P., Marsch, E., & Mann, G. 2000, A&A, 360, 1139
Harmon, J. K., & Coles, W. A. 2005, JGRA, 110, 3101
Heinemann, M., & Olbert, S. 1980, JGR, 85, 1311
Hollweg, J. V., Cranmer, S. R., & Chandran, D. G. 2010, ApJ, 722, 1495
Hollweg, J. V., Kagashvili, E. Kh., & Chandran, B. D. G. 2013, ApJ, 769, 142

Isenberg, P. A., & Lee, M. A. 1996, JGR, 101, 11055
Jewitt, D. 1997, EM&P, 79, 35
Klimchuk, J. A. 2012, JGR, 117, 12102
Knight, M. M., A'Hearn, M. F., Biesecker, D. A., et al. 2010, AJ, 139, 926
Krishna Prasad, S., Banerjee, D., Van Doorsselaere, T., & Singh, J. 2012, A&A, 546, 50
Landi, E., Young, P. R., Dere, K. P., Del Zanna, G., & Mason, H. E. 2013, ApJ, 763, 86
Lee, M. A., & Roberts, B. 1986, ApJ, 301, 430
Lemen, J. R., Title, A. M., Akin, D. J., et al. 2012, SoPh, 275, 17
Marsden, B. 2005, ARA&A, 43, 75
McCauley, P., Saar, S. H., Raymond, J. C., Ko, Y.-K., & Saint-Hilaire, P. 2013, ApJ, 768, 161
Mecheri, R., & Marsch, E. 2008, A&A, 481, 853
Moebius, E., Hovestadt, D., Klecker, B., Scholer, M., & Gloeckler, G. 1985, Natur, 318, 426
Nakariakov, V. M., Roberts, B., & Murawski, K. 1998, A&A, 332, 795
Newkirk, G., Jr., & Harvey, J. 1968, SoPh, 3, 321
November, L. J., & Koutchmy, S. 1996, ApJ, 466, 512
Ofman, L., Nakariakov, V. M., & DeForest, C. E. 1999, ApJ, 514, 441
Orrall, F. Q., Rottman, G. J., Fisher, R. R., & Munro, R. H. 1990, ApJ, 349, 656
Pereira, T. M. D., De Pontieu, B., & Carlsson, M. 2012, ApJ, 759, 18

Phaneuf, R. A., Janev, R. K., & Pindzola, M. S. 1987, Oak Ridge National Laboratory Report ORNL-6090, http://www-cfadc.phy.ornl.gov/redbooks/five/5.html
Poedts, S., Rogava, A. D., & Mahajan, S. M. 1998, ApJ, 505, 369
Raymond, J. C., Uzzo, M., Ko, Y.-K., et al. 1998, ApJ, 564, 1054
Saito, K. 1965, PASJ, 17, 1
Saleem, H., Ali, S., & Poedts, S. 2012, ApJ, 748, 90
Sankrit, R., Williams, B. J., Borkowski, K. J., et al. 2010, ApJ, 712, 1092
Schultz, D. R., Krstic, P. S., Lee, T. G., & Raymond, J. C. 2008, ApJ, 678, 950
Schwadron, N. A., Fisk, L. A., & Zurbuchen, T. H. 1999, ApJ, 521, 859
Sekanina, Z., & Chodas, P. W. 2012, ApJ, 757, 127
Spitzer, L. 1968, Diffuse Matter in Space (New York: Interscience)
Stein, R. F. 1971, ApJS, 22, 419
Suess, S. T. 1982, SoPh, 75, 145
Threlfall, J., De Moortel, I., McIntosh, S. W., & Bethge, C. 2013, A&A, 556, 124
Tian, H., McIntosh, S. W., Habbal, S. R., & He, J. 2011, ApJ, 736, 130
Uzzo, M., Raymond, J. C., Biesecker, D., et al. 2001, ApJ, 558, 403
Valley, G. C. 1974, ApJ, 188, 181
Williams, L. L., & Zank, G. P. 1994, JGR, 99, 19229
Woo, R. 2007, SoPh, 241, 251
Young, P. R., Klimchuk, J. A., & Mason, H. E. 1999, A&A, 350, 286
Zank, G. P., Jetha, N., Hu, Q., & Hunana, P. 2012, ApJ, 756, 21